Article

Effect of Ag Modification on the Structure and Photocatalytic Performance of TiO$_2$/Muscovite Composites

Fengqiu Qin [1], Ling Zhang [1], Yuhao Luo [2], Lili He [1], Shiji Lu [1], Li Xu [1], Xiaodong Zhu [1,2,*] and Wei Feng [1,*]

1 School of Mechanical Engineering, Chengdu University, Chengdu 610106, China
2 College of Materials and Chemistry & Chemical Engineering, Chengdu University of Technology, Chengdu 610051, China
* Correspondence: xiaodangjia21@126.com (X.Z.); fengwei233@126.com (W.F.)

Abstract: Ag/TiO$_2$/muscovite (ATM) composites were prepared by the sol–gel method and the effects of Ag modification on the structure and photocatalytic performance were investigated. The photocatalysts were characterized using X-ray diffraction (XRD), scanning electron microscopy (SEM), transmission electron microscopy (TEM), Brunauer–Emmett–Teller surface area (BET), X-ray photoelectron spectroscopy (XPS), Fourier transform infrared spectra (FTIR), photoluminescence spectra (PL) and ultraviolet–visible diffuse reflectance spectra (DRS). The photocatalytic activity of the obtained composites was evaluated by taking 100 mL (10 mg/L) of Rhodamine B (RhB) aqueous solution as the target pollutant. The muscovite (Mus) loading releases the agglomeration of TiO$_2$ particles and the specific surface area increases from 17.6 m^2/g (pure TiO$_2$) to 39.5 m^2/g (TiO$_2$/Mus). The first-order reaction rate constant increases from 0.0009 min^{-1} (pure TiO$_2$) to 0.0074 min^{-1} (150%TiO$_2$/Mus). Ag element exists in elemental silver. The specific surface area of 1-ATM further increases to 66.5 m^2/g. Ag modification promotes the separation of photogenerated electrons and holes and increases the visible light absorption. 1%Ag-TiO$_2$/Mus (1-ATM) exhibits the highest photocatalytic activity. After 100 min, the rhodamine B (RhB) degradation degrees of PT, 150%TiO$_2$/Mus and 1-ATM are 10.4%, 48.6% and 90.6%, respectively. The first-order reaction rate constant of 1-ATM reaches 0.0225 min^{-1}, which is 25 times higher than that of pure TiO$_2$.

Keywords: TiO$_2$; muscovite; Ag modification; photocatalytic activity

1. Introduction

Rhodamine B (RhB) is a typical dye organic compound which is primarily used for industrial dyeing. RhB possesses carcinogenicity and teratogenicity, causing certain harm to human health and the sustainable development of ecosystems when it is discharged into water bodies [1,2]. The methods of removing RhB include physical adsorption, chemical precipitation, biological filtration, etc. [3–5]. Because photocatalysts are able to degrade organic dyes into small inorganic molecules such as water and carbon dioxide directly under the irradiation of a light source without producing secondary pollution, this green technology has attracted wide attention [6–9]. Among numerous semiconductor photocatalyst materials, TiO$_2$ has received the most extensive research due to its low cost, stable chemical properties, non-toxicity and harmlessness [10–14]. However, nanoscale TiO$_2$ tends to readily aggregate, which results in a reduction in active reaction sites and adsorption performance. Using a matrix to load TiO$_2$ can effectively reduce the agglomeration between particles, increasing the specific surface area and providing more reaction sites [15–18]. Muscovite (Mus) possesses the advantages of low price, acid and alkali resistance, heat resistance and chemical stability, and is commonly employed to load TiO$_2$ to release its agglomeration [19–22]. Li [21] et al. prepared TiO$_2$/Mus using a hydrothermal method and found that the particles' agglomeration released after loading on Mus, which is beneficial to advancing photocatalytic performance.

On the other hand, the band gap width of TiO_2 is large (3.2 eV), meaning it is only active in the ultraviolet light range with short wavelengths, limiting its applicability in the visible light range. In addition, the rapid recombination of photogenerated charges reduces photocatalytic activity [10,23]. Therefore, it is necessary to modify TiO_2 to improve its photocatalytic performance. Ion doping, semiconductor coupling and noble metal decoration are common modification methods [24–26]. Feng et al. [14] prepared Fe/N co-doped nano-TiO_2 using the solvothermal method and the degradation degree of RhB increased from 57.4% (pure TiO_2) to 96.2% after irradiation for 60 min. The co-doping of Fe and N elements reduced the band gap width, which broadened the visible light response range, improving photocatalytic activity. Akhter et al. [25] synthesized ZnO/TiO_2 composites using the sol–gel method and the degradation degree of MB reached 96% after illumination for 3 h. The combination of ZnO and TiO_2 forms II-type semiconductor junctions which promote the separation of photogenerated electrons and holes, improving quantum utilization. Because the work functions of noble metals are larger than that of TiO_2, when they make contact to form Schottky junctions, the photogenerated electrons generated by TiO_2 are transferred to noble metals. Due to the existence of Schottky junctions, electrons in noble metals are prevented from flowing back into TiO_2, which promotes the separation of photogenerated charges [27–30]. Additionally, owing to the surface plasmon resonance effect, noble metal modification can enhance the absorption in the visible light region, advancing the photocatalytic performance [31–33]. Bamola et al. [26] prepared Au-TiO_2 using an inert gas evaporation method and it was found that Au and TiO_2 formed Schottky junctions which favored the separation of photogenerated electrons and holes, inhibiting the recombination of carriers. Meanwhile, the absorption of composite materials in the visible light region was enhanced by Au decoration, which promoted the photocatalytic performance.

In this study, to combine the advantages of muscovite loading, which alleviates the agglomeration of TiO_2 particles, and noble metal modification, which enhances the quantum utilization and visible light absorption simultaneously, Ag-modified and Mus-loaded TiO_2 composite materials were prepared using a sol–gel method. The crystal structure, surface morphology, specific surface area, elemental composition, valence state and optical properties of the composite photocatalysts were analyzed with XRD, SEM, TEM, BET, XPS, FTIR, PL and RDS. The photocatalytic activity was evaluated by measuring the degradation degree of RhB and the mechanism of improving the photocatalytic performance with Mus loading and Ag modification was discussed.

2. Results and Discussion

2.1. Phase Composition

Figure 1 shows the XRD patterns of pure TiO_2 (PT), 150%TiO_2/Mus (TM) and Ag/TiO_2/muscovite (ATM). The three strong peaks in the XRD diffraction pattern of Mus appearing at 8.9°, 26.8° and 45.5° correspond to the (002), (006) and (029) crystal planes. The diffraction peaks of PT at 2θ = 25.3°, 37.8° and 48.1° correspond to the (101), (004) and (200) crystal planes of anatase, respectively, which means that TiO_2 is single-phase anatase [32,34]. The diffraction peaks of anatase and Mus appear in the pattern of TM simultaneously, indicating that TiO_2/Mus composites are formed. After Ag modification, diffraction peaks at 2θ = 38.1°, indexed to the (111) crystal plane of metallic Ag, can be detected, indicating that Ag/TiO_2/muscovite composites are obtained [35,36]. With the increase in Ag content, the diffraction peak intensity of the (111) plane is enhanced. Figure S1 shows the XRD patterns of PT and TiO_2/Mus. As the content of Mus increases from 15% to 200%, the intensity of the Mus diffraction peaks increases, while the intensity of the TiO_2 diffraction peaks decreases and the half-height width expands gradually, implying that Mus loading increases the amorphous composition and decreases the crystallinity of TiO_2.
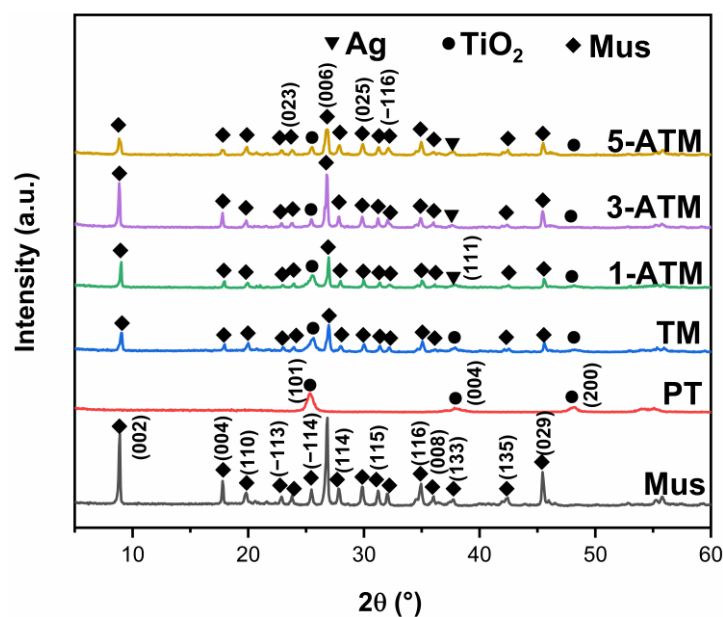
Figure 1. XRD patterns of samples.

2.2. Morphology and BET Surface Area

Figure 2 shows the SEM images of samples. As can be seen in Figure 2a, Mus particles present flaky shapes. It is observed in Figure 2b that PT prepared with the sol–gel method shows a significant agglomerative phenomenon, and the particle sizes are massive. When the Mus/TiO_2 mass ratio is 150%, it can be observed in Figure 2c that TiO_2 particles are evenly distributed on the surface of Mus, which reduces the aggregation of TiO_2. Figure S2 shows the SEM images of 15%TiO_2/Mus and 200%TiO_2/Mus, from which it can be seen that with increasing Mus content, the agglomeration of TiO_2 particles reduces more clearly. In Figure 2d, ATM shows comparable morphology to TM, which suggests that Ag modification does not cause the re-aggregation of TiO_2 particles.

Figure 3 shows the TEM and HRTEM images of 1-ATM. As can be seen in Figure 3a, TiO_2 particles are dispersed on the Mus matrix and the size of a single particle ranges from 10 to 20 nm. Figure 3b shows the HRTEM image of 1-ATM. The marked crystal plane spacing of 0.351 nm is indexed to the anatase (101) crystal plane [21,37]. The lattice fringe of 0.228 nm can be ascribed to the crystal face of Ag (111) [38,39], indicating that Ag element exists as metallic Ag, which is consistent with the XRD results.
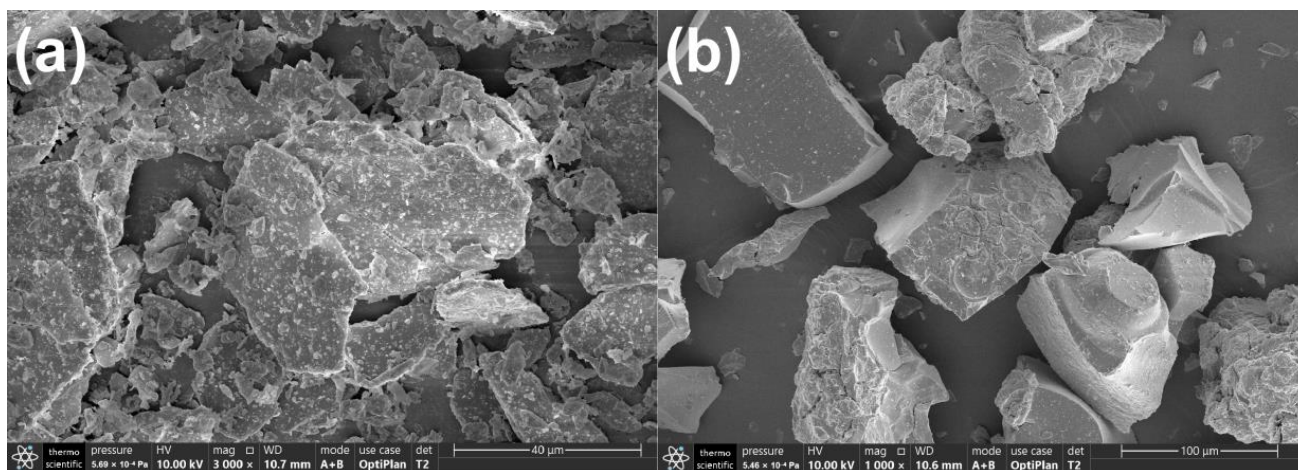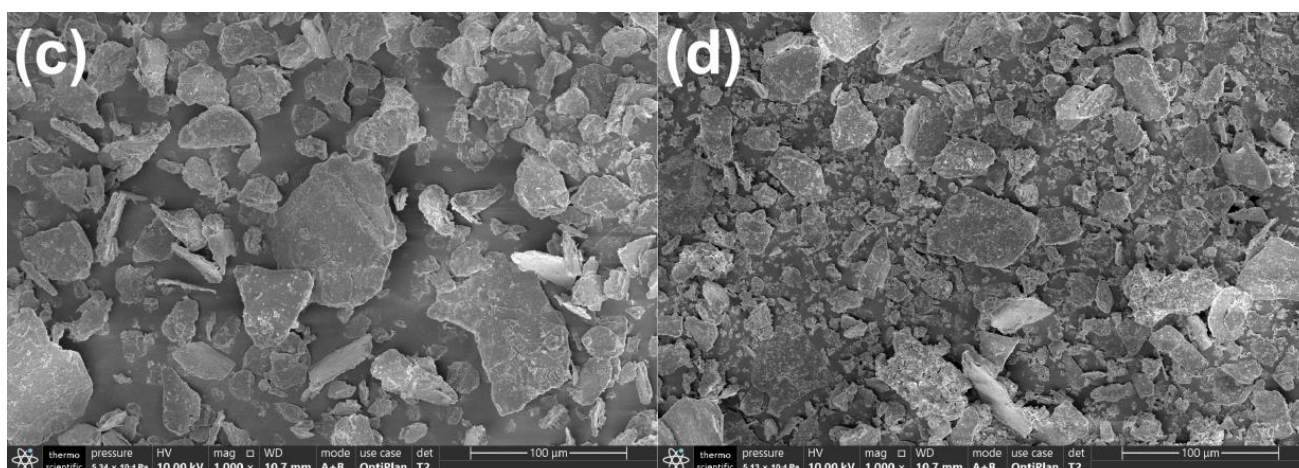

Figure 2. *Cont.*

Figure 2. SEM images of Mus (**a**), PT (**b**), TM (**c**) and 1-ATM (**d**).
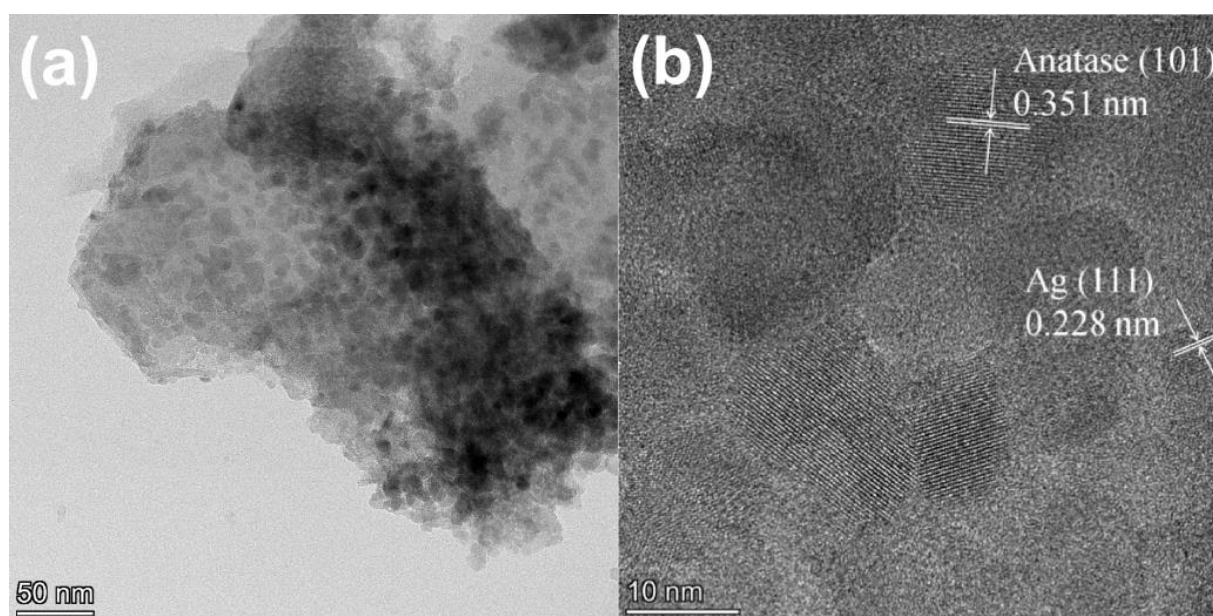

Figure 3. TEM (**a**) and HRTEM (**b**) images of 1-ATM.

Figure 4 shows the N_2 adsorption–desorption isotherms of PT, TM and 1-ATM. The specific surface area of PT is 17.6 m^2/g. When it is loaded on Mus, the specific surface area increases to 39.5 m^2/g (TM), indicating that the aggregation phenomenon of TiO_2 particles is reduced after Mus loading. Ag modification further increases the specific surface area (66.5 m^2/g) of 1-ATM. The increase in surface area provides more active sites for the photocatalytic reaction, which is beneficial to photocatalytic performance [15,16,22].

2.3. Element Valence State

Figure 5 shows the XPS spectra of 1-ATM. The signal peaks of Ti, O and Ag elements appear in the total spectrum (Figure 5a). Figure 5b shows the high-resolution spectrum of Ti 2p. The two peaks at 458.0 and 463.5 eV are indexed to Ti $2p_{3/2}$ and Ti $2p_{1/2}$, indicating that Ti element exists in the form of 4+ [32,40,41]. The high-resolution spectrum of O 1s is shown in Figure 5c. The two peaks at 529.8 and 531.1 eV correspond to lattice oxygen (O^{2-}) and surface hydroxyl (OH^-) [42,43].
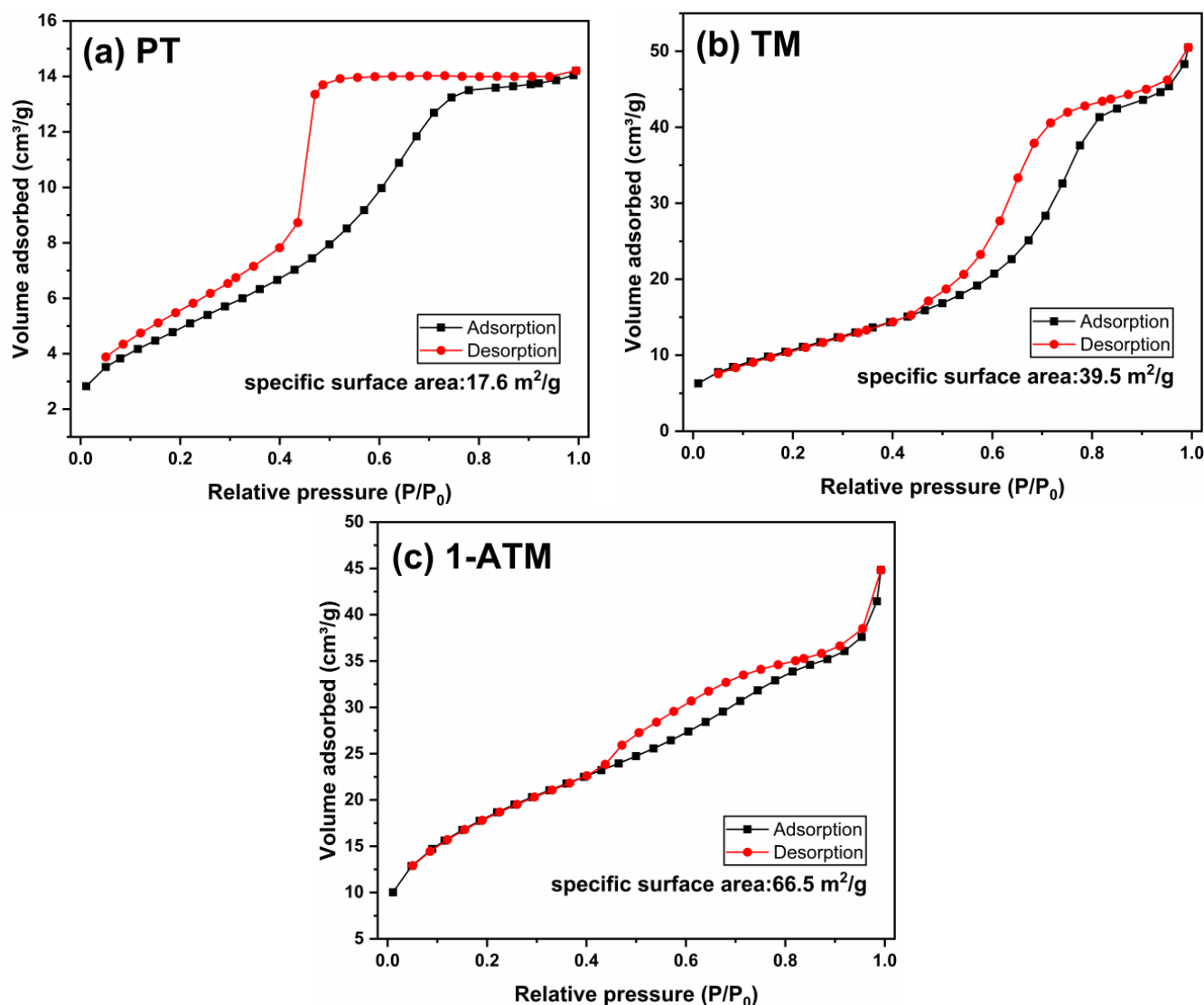
Figure 4. Nitrogen adsorption–desorption isotherms of PT (**a**), TM (**b**) and 1-ATM (**c**).

2.4. FTIR Analysis

Figure 6 shows the FTIR spectra of PT, Mus, TM and 1-ATM. Mus shows a relatively obvious absorption band in the high-frequency region and the broad absorption band at 3608 cm^{-1} can be attributed to the Al-O-H stretching vibration [44]. The peak at 1632 cm^{-1} corresponds to the O-H bending vibration [32]. In addition, the wavelength of 1105 cm^{-1} corresponds to the asymmetric tensile vibration peak of Si-O-Si, indicating the existence of a SiO$_2$ skeleton structure in Mus [45,46]. The weak peaks at 922 cm^{-1} are caused by the asymmetric tensile vibration of Si-O-Ti in Mus [45]. The absorption peak at 787 cm^{-1} corresponds to the vibration of the hydroxyl group of Mg-Al-OH in Mus, indicating that the structure of Mus has not been damaged by heat treatment. In PT, an obvious absorption peak is observed near wavelength 1401 cm^{-1}, which is formed by the stretching mode of metal Ti ions and the absorption of atmospheric CO$_2$ by carbonyl (C=O) [10]. Significantly, compared to Mus, the corresponding absorption peaks are also observed in TM and 1-ATM, which can be ascribed to the interaction between TiO$_2$, Mus and Ag. There is no peak related to Ag that can be detected, which may be because Ag levels are too low for the instrument to detect.
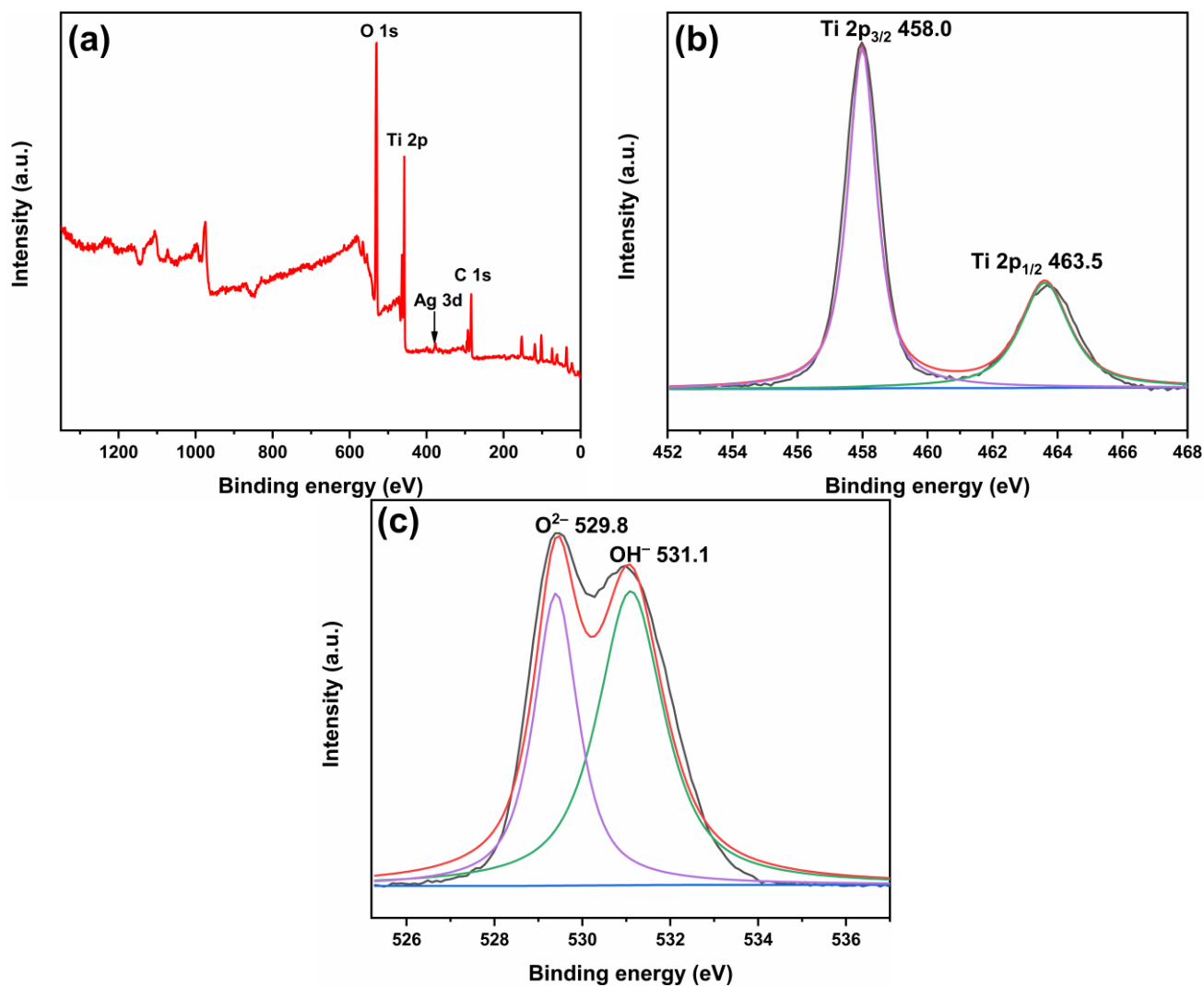
Figure 5. XPS spectra of 1-ATM: total spectrum (**a**), Ti 2p (**b**) and O 1s (**c**).
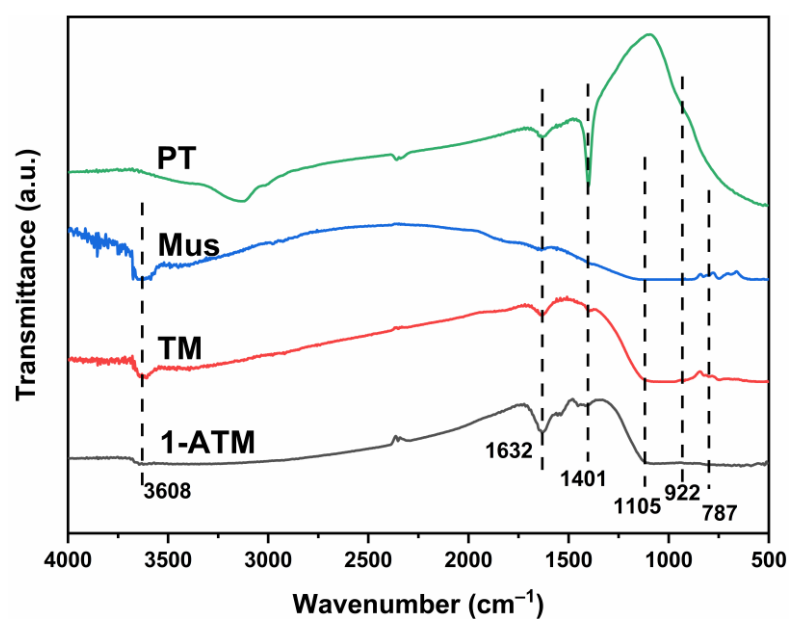

Figure 6. FTIR spectra of PT, Mus, TM and 1-ATM.

2.5. Optical Property

The separation of photogenerated electrons and holes is the core step of photodegradation. The higher the separation rate of photoinduced charge is, the more free radicals are generated during the degradation process, which is beneficial to the photocatalytic performance [36,42]. The photoluminescence (PL) peaks come from the released photons when the photogenerated electrons and holes recombine. Therefore, the lower PL peak intensity indicates a lower recombination of the photogenerated charges [47–49]. Figure S3 shows PL spectra of PT and TiO_2/Mus in the wavelength range of 350–550 nm. It can be seen that the peak intensity of TiO_2/Mus increases gradually when the loading amount of Mus increases from 15% to 200%, indicating that Mus loading aggravates the recombination of photogenerated charges. The XRD results show that the higher the Mus loading, the lower the TiO_2 diffraction peak intensity, resulting in a decrease in TiO_2 crystallinity and an increase in amorphous components and crystal defects which may become the recombination centers for photogenerated charges, thus increasing the PL peak intensity [22,50]. Figure 7 shows the PL spectra of PT, TM and ATM. After Ag modification, the recombination of photogenerated electrons and holes in ATM decreases compared to PT and TM. As the Fermi level of Ag is at the base of the TiO_2 conduction band, the photogenerated electrons on the TiO_2 conduction band transfer to the surface of Ag, which promotes the separation of photoinduced charges and improves quantum efficiency [35,51]. Significantly, when the concentration of Ag is excessive (5%), the PL peak intensity rises, which may be due to the formation of new recombination centers after superfluous Ag modification [43,52].
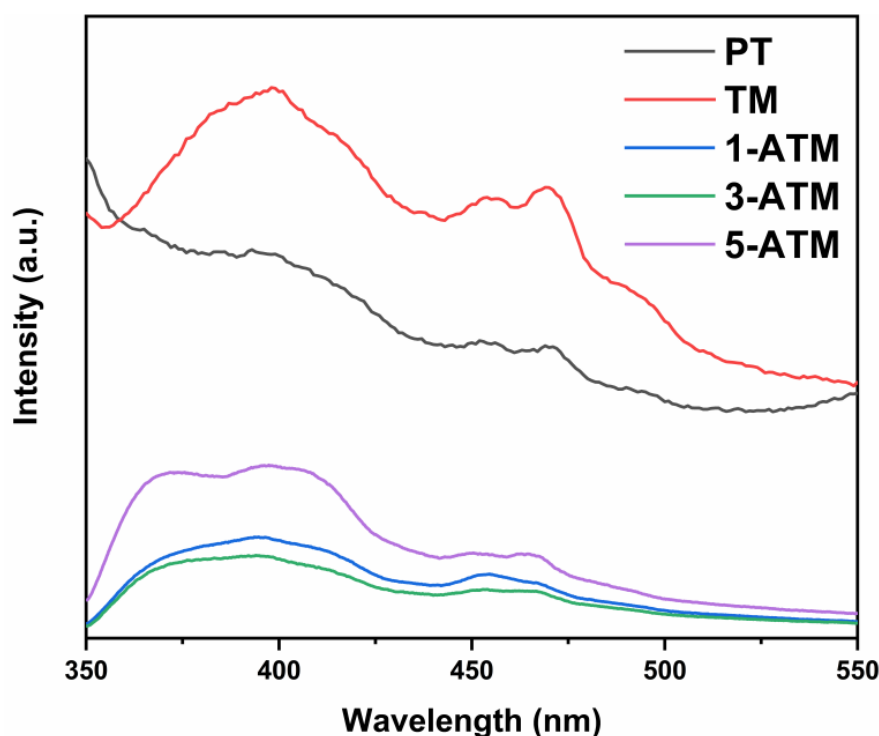

Figure 7. Photoluminescence spectra of PT, TM and ATM.

Figure 8 shows the UV–visible absorption spectra (a) and the band gap (b) of PT, TM and 1-ATM. As shown in Figure 8a, compared with PT, the absorption edge of TM and 1-ATM red shifts, indicating that Mus loading and Ag modification favor the utilization of visible light. The specific forbidden band width can be calculated as follows [52–54]:

$$\alpha h\upsilon = A(h\upsilon - Eg)^{1/n} \tag{1}$$

where h, υ, A and *Eg* are the Planck constant, the incident photon frequency, the proportional constant and the band gap (*Eg*), respectively. The value of n is related to the type of semiconductor, which is 2 for indirect semiconductors and is 1/2 for direct semiconductors [53,54]. Therefore, the value of *Eg* can be determined by the $(\alpha h\upsilon)^{1/2}$-$h\upsilon$ curves in Figure 8b, which show that the band gaps of PT, TM and 1-ATM are 3.10, 3.06 and 2.89 eV, respectively. Ag modification diminishes the band gap of TiO_2, reduces the energy barrier during the electron transition and promotes light absorption in the visible region.
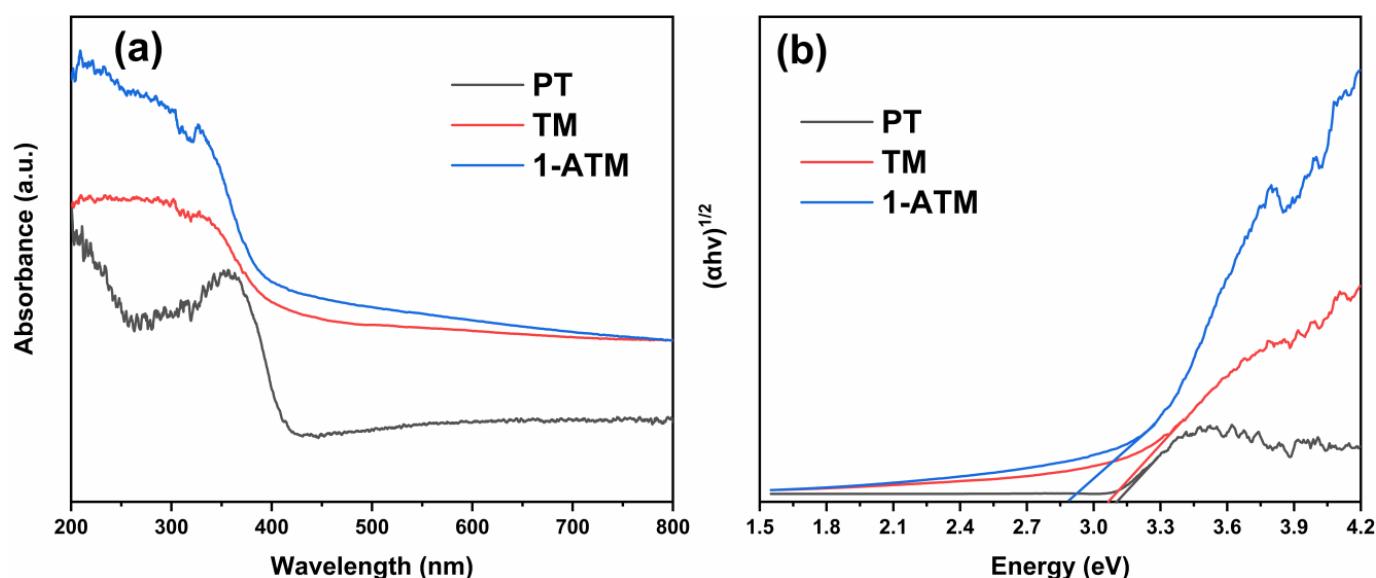

Figure 8. UV–visible absorption spectra (**a**) and band gap (**b**) of PT, TM and 1-ATM.

2.6. Photocatalytic Performance

Figure S4 presents the RhB degradation degrees of PT and TiO_2/Mus, which show that TiO_2/Mus exhibits the highest degradation degree when the Mus/TiO_2 mass ratio is 150%. Figure 9a gives the RhB degradation degree curves of PT, TM and ATM. After 100 min, the degradation degrees of PT, TM, 1-ATM, 3-ATM and 5-ATM are 10.4%, 48.6%, 90.6%, 64.6% and 45.6%. Evidently, when TiO_2 is loaded on Mus, the photocatalytic activity is significantly improved, which can be ascribed to the fact that the greater dispersion of TiO_2 particles significantly enhances the specific surface area and provides more reactive sites. Moreover, Ag modification further advances the photocatalytic performance of TiO_2/Mus composites. Combining PL and DRS spectra results, the enhancement of photocatalytic activity can be explained such that Ag modification reduces the recombination of photogenerated electrons and holes and enhances the absorption of visible light. The amount of Ag addition is the key to photocatalytic activity. ATM exhibits the highest photocatalytic activity when the Ag/Ti molar ratio is 1%. When the concentration of Ag is excessive, new recombination centers for photogenerated electrons and holes are formed, which is not conducive to the separation of photogenerated charges [43,52]. On the other hand, significant Ag deposition will cover the surface of TiO_2 particles and hinder the absorption of the light source, reducing the photocatalytic degradation efficiency [39,55,56]. Figure 9b shows the kinetics curves of samples. The first-order reaction rate constants of PT, TM, 1-ATM, 3-ATM and 5-ATM are 0.0009, 0.0074, 0.0225, 0.0088 and 0.0039 min^{-1}, respectively. 1-ATM produces the fastest reaction rate, which is in line with the degradation results.

To study the reusability of 1-ATM, the RhB degradation cycle experiment was carried out and the results are shown in Figure 10. After four cycles, the degradation degree of 1-ATM is 80.2%, which is slightly lower than 90.6%, indicating that 1-ATM has relatively considerable reusability.
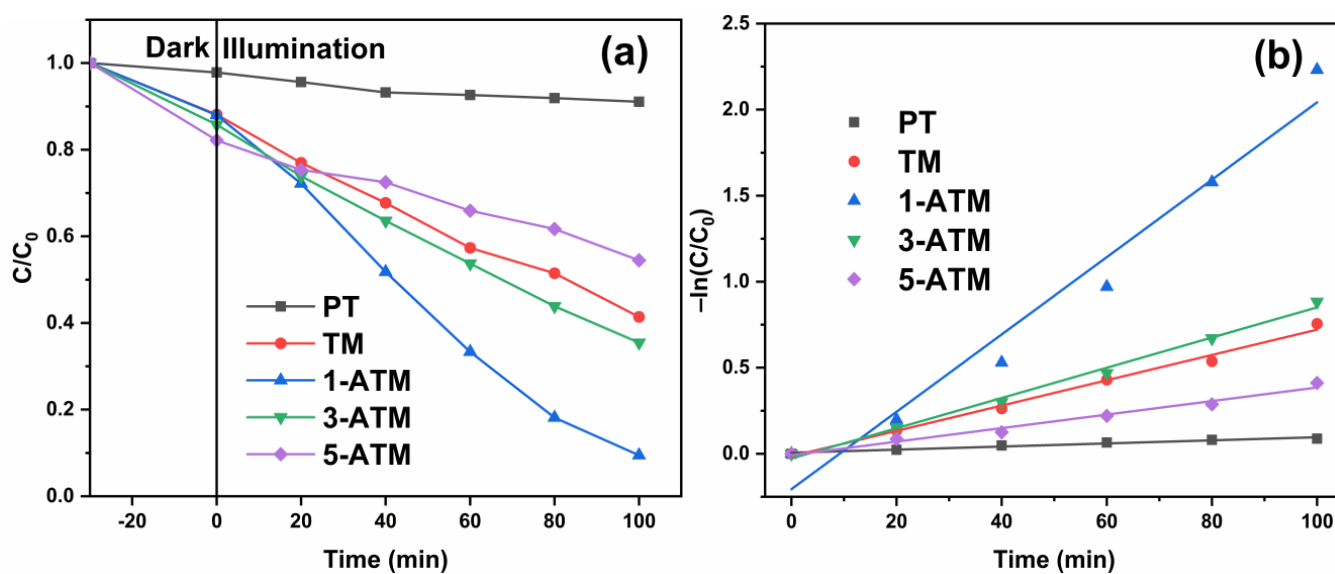
Figure 9. Degradation degree curves (**a**) and kinetics curves (**b**) of PT, TM and ATM.
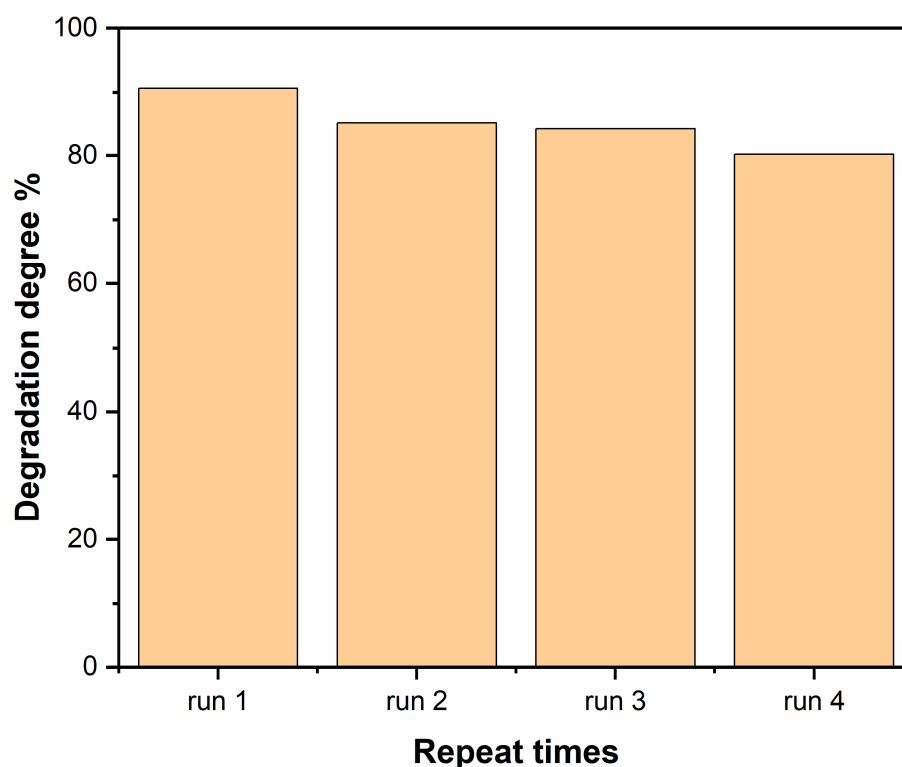

Figure 10. The reuse experiment of 1-ATM photocatalyst for RhB degradation.

The XRD patterns of the fresh and used 1-ATM composite photocatalysts are shown in Figure 11. Compared to the initial sample, the positions of the diffraction peaks do not change and the peak intensities decrease marginally, which can be attributed to a small amount of undegraded RhB molecules remaining on the surface of 1-ATM [35].

To further verify the stability of 1-ATM, the FTIR spectra of the fresh and used 1-ATM are shown in Figure 12. Compared to the fresh spectrum, except for a slight decrease in peak strength, the characteristic peaks of the used sample can still be observed and have not shifted, indicating that the structure of the 1-ATM composite material is relatively stable.
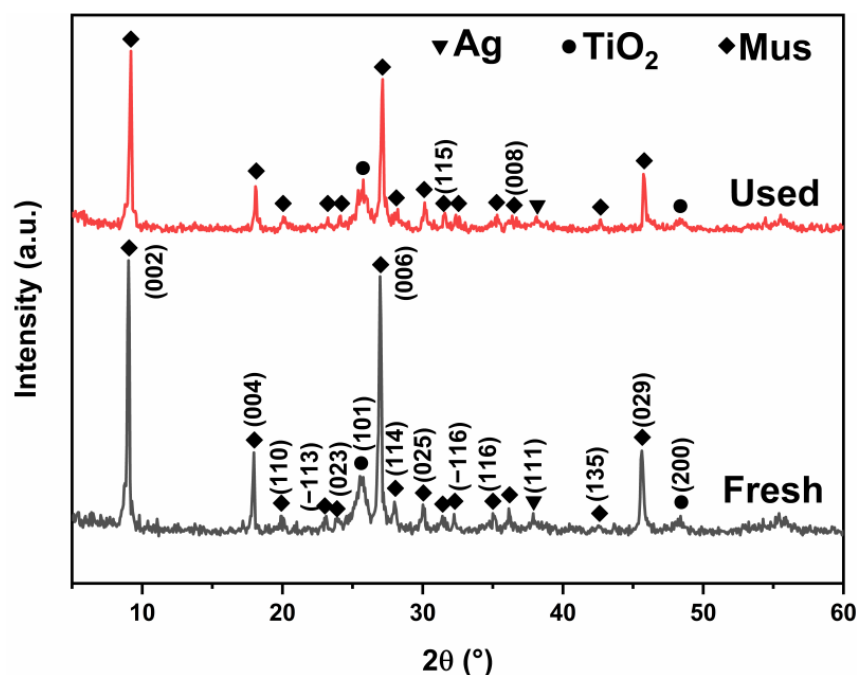
Figure 11. XRD patterns of 1-ATM photocatalyst before and after the photocatalytic experiment.
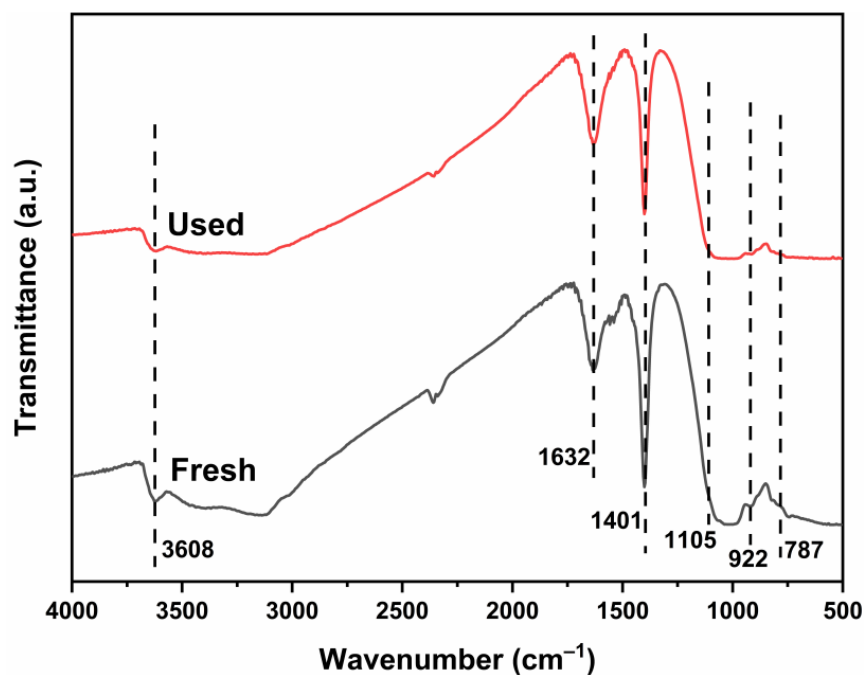

Figure 12. FTIR spectra of 1-ATM photocatalyst before and after the photocatalytic experiment.

2.7. Photocatalytic Degradation Mechanism

To determine the active species in the photodegradation process of 1-ATM, active species inhibition experiments were carried out on strong oxidizing groups such as h^+, $\cdot O_2^-$ and $\cdot OH$, and the results are as shown in Figure 13. Based on the RhB degradation system, 2 mL of p-benzoquinone (BQ, $\cdot O_2^-$ trapping agent), isopropyl alcohol (IPA, $\cdot OH$ trapping agent) or ammonium oxalate (AO, h^+ trapping agent) was added to determine the active substances [57–59]. The degradation degrees of RhB are BQ (40.2%) < AO (62.9%) < IPA (67.9%) < no scavenger (90.6%), which indicates that $\cdot O_2^-$ is the main active group, while $\cdot OH$ and h^+ are secondary groups.
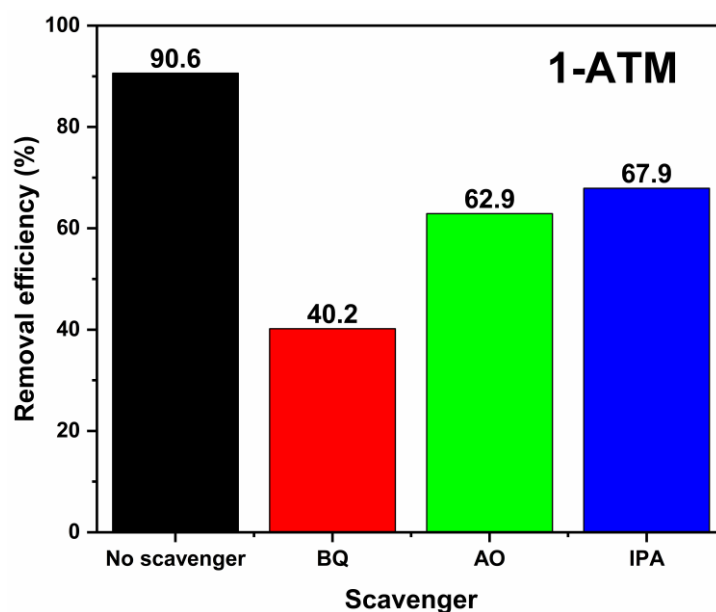
Figure 13. Degradation degrees of 1-ATM in the presence of different scavengers.

Using the characterization and photocatalytic degradation experiment results, the mechanism of photodegradation of RhB with the 1-ATM composite photocatalyst is proposed, as shown in Figure 14. Ag-TiO$_2$ is firmly fixed on the surface of Mus using chemical bond links, which releases the agglomeration of TiO$_2$ particles and provides more active reaction sites. When the photocatalysts are exposed to light irradiation in the ultraviolet region, electrons in the TiO$_2$ valence band are excited to the conduction band, forming photogenerated electrons while leaving holes in the valence band. Photogenerated electrons with reducibility undergo a reduction reaction with O$_2$ molecules adsorbed on the particle's surface to generate ·O$_2^-$ radicals. Meanwhile, holes react with groups such as H$_2$O and OH$^-$ to generate ·OH radicals [3,25]. After Ag modification, as the work function of TiO$_2$ is smaller than that of metal silver, electrons in TiO$_2$ flow into metal Ag, while accumulating positive charges on TiO$_2$. The accumulation of negative charges in metal Ag and positive charges in TiO$_2$ creates a built-in electric field directed from TiO$_2$ to metal Ag and causes the TiO$_2$ energy band to bend upward, forming a Schottky barrier [27,30]. Electrons in Ag particles are prevented from flowing back to TiO$_2$, owing to the existence of Schottky barriers. In the subsequent photocatalytic reaction, electrons accumulated on the metal Ag surface undergo a reduction reaction and holes accumulated in TiO$_2$ undergo an oxidation reaction, leading to a new equilibrium state of the Fermi energy levels between metal Ag and TiO$_2$ [29,30].

In the visible region, TiO$_2$ valance band electrons cannot be excited. However, when metal Ag undergoes irradiation, a surface plasmon resonance effect occurs, causing free electrons to rise from their initial thermal equilibrium state to a higher energy state, increasing the energy of free electrons, which are then called hot electrons [30]. The yielded hot electrons will transfer to the TiO$_2$ conduction band if their energies are greater than the conduction band potential of TiO$_2$. This excitation mechanism does not need the photon energy to be greater than the TiO$_2$ band gap, but only needs to meet the requirement of $h\upsilon \geq E_f - E_c$ (E_c is the conduction band potential of TiO$_2$ and E_f is the Fermi energy level when TiO$_2$ and Ag reach an equilibrium state) [30]. In general, the necessary photon energy is smaller than the TiO$_2$ band gap, making it more advantageous to use light sources for photocatalytic processes in the long wavelength range. Due to the existence of Schottky energy barriers, hot electrons that have been transferred to the TiO$_2$ conduction band cannot flow back to the metal Ag [27–30]. When hot electrons are injected into the TiO$_2$ conduction band, the corresponding thermal holes remain on Ag particles, causing an oxidation reaction.
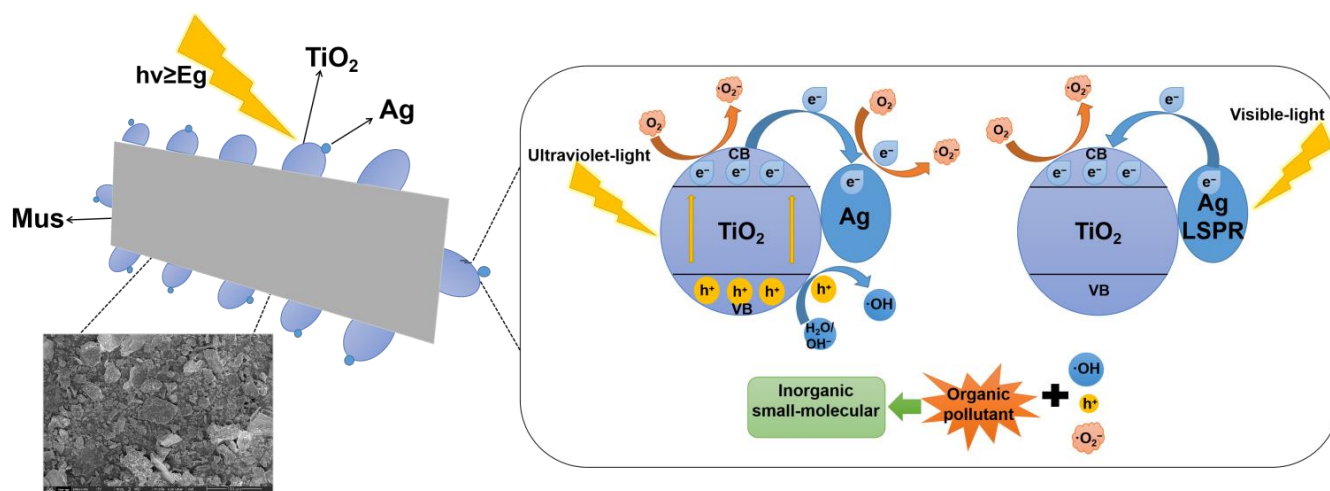
Figure 14. Schematic diagram of charge transfer and photodegradation of RhB for 1-ATM.

3. Materials and Methods

3.1. Sample Preparation

Butyl titanate ($C_{16}H_{36}O_4Ti$, AR, $\geq98.0\%$), anhydrous ethanol (CH_3CH_2OH, AR, $\geq99.7\%$), glacial acetic acid ($C_2H_4O_2$, AR, $\geq99.5\%$), silver nitrate ($AgNO_3$, AR, $\geq99.8\%$) and Rhodamine B (RhB) ($C_{28}H_{31}N_2O_3Cl$, AR, $\geq99.0\%$) were purchased form Chengdu Kelon Chemical Reagent Factory (PR China).

Muscovite (Mus) acid treatment: First, 11.98 g Mus was placed in a beaker which was filled with 20 mL deionized water and 40 mL glacial acetic acid. The suspension was continuously stirred for 60 min and then washed repeatedly with deionized water and anhydrous ethanol. Finally, the sample was obtained for use after drying.

Pure TiO_2: In total, 74 mL anhydrous ethanol and 34 mL tetrabutyl titanate were added into a beaker and stirred evenly to obtain solution A. Then, 8 mL deionized water, 7 mL glacial acetic acid and 37 mL anhydrous ethanol were mixed evenly to obtain solution B. A separating funnel was used to slowly drop solution B into solution A and stirring was maintained until sol was formed. After aging, the sol converted to gel, which was heat-treated at 450 °C for 1h in a muffle furnace to obtain TiO_2. Pure TiO_2 was labeled as PT.

TiO_2/Mus: The acid-treated muscovite was added into the TiO_2 sol under the condition of magnetic stirring and the other preparation steps were the same as above. The TiO_2/Mus composite (Mus/TiO_2 mass ratio = 150%) was labeled as TM.

Ag-TiO_2/Mus: $AgNO_3$ was added to solution B and the other preparation steps were the same to produce Ag-TiO_2/Mus. The molar ratios of Ag/Ti were 1%, 3% and 5%. The Ag-TiO_2/Mus samples were labeled as 1-ATM, 3-ATM and 5-ATM.

3.2. Sample Characterization

The crystal structure and composition of samples were analyzed using a DX-2700 X-ray diffractometer. Cu Kα radiation was used as an X-ray source, with a scanning range of 5–60° and a scanning speed of 0.06°/s (XRD, Dandong Haoyuan Instrument Co. Ltd., Dandong, China). The microscopic morphology of samples was studied with a Hitachi SU8220 scanning electron microscope (SEM) and a JEM-F200 transmission electron microscope (TEM and HRTEM) (FEI Company, Hillsboro, OR, USA). A V-sorb 2800S analyzer was used to measure the specific surface area (BET, Guoyi Precision Measurement Technology Co. Ltd., Beijing, China). The elements' valence states were analyzed with XSAM800-type X-ray photoelectron spectroscopy (XPS, Thermo Scientific K-Alpha, Kratos Ltd., Manchester, UK). The photoluminescence spectra were measured with an F-4600 fluorescence spectrum analyzer with a Xe lamp at an excitation wavelength of 300 nm (PL, Shimadzu Group Company, Kyoto, Japan). The light absorption was analyzed with a

UV-3600 UV–visible spectrophotometer (DRS, Shimadzu Group Company, Kyoto, Japan). An Agilent Cary630 Fourier transform infrared spectrometer was used to analyze the bonding condition (FTIR, Shanghai Weiyi Biotechnology Co. Ltd., Shanghai, China).

3.3. Photocatalysis Experiment

The photocatalytic activity of samples was evaluated by measuring the decomposition of RhB as a model pollutant. A combination of 100 mL (10 mg/L) RhB and 0.1 g sample was mixed in a beaker. The mixture was ultrasonically dispersed for 10 min and then stirred for 30 min under dark conditions to achieve the adsorption and desorption equilibrium. A xenon lamp was used as the light source and the samples were collected every 20 min. After centrifuging, the absorbance of the obtained solution was tested at the wavelength of 553 nm. The degradation degree of RhB was calculated using the formula $(A_0 - A_t)/A_0 \times 100\%$, where A_0 and A_t are the initial absorbance and t time absorbance.

4. Conclusions

TiO_2/Mus composites were prepared using the sol–gel method and modified by Ag decoration. The agglomeration of TiO_2 particles is reduced by Mus loading and the specific surface area is further increased after the addition of Ag, both of which provide more active sites for photocatalytic degradation reactions. Ag-TiO_2 is firmly fixed on the surface of the Mus matrix by chemical bond links between TiO_2 and Mus. ATM has much lower PL peak intensity than PT and Mus because Ag modification reduces the recombination of photogenerated charges. Ag modification also enhances the absorption in the visible light region. The degradation degree of RhB was employed to evaluate the photocatalytic performance of samples. The photocatalytic activity of 1-ATM is the highest and the degradation degree of RhB is 90.6% after illumination for 100 min, which is higher than that of pure TiO_2 (10.4%). The first-order reaction rate constant of 1-ATM reaches 0.0225 min^{-1}, which is 25 times higher than that of pure TiO_2 (0.0009 min^{-1}). The active species experiment using 1-ATM shows that $\cdot O_2^-$ radicals play a major role in the photodegradation process.

References

1. Chen, Y.M.; Pu, S.L.; Wang, D.Y.; Zhang, Y.C.; Wan, G.J.; Zhao, Q.; Sun, Y. Facile synthesis of AgBr@ZIF-8 hybrid photocatalysts for degradation of Rhodamine B. *J. Solid State Chem.* **2023**, *321*, 123857. [CrossRef]
2. Nazir, M.A.; Najam, T.; Jabeen, S.; Wattoo, M.A.; Bashir, M.S.; Shah, S.S.A.; Rehman, A.U. Facile synthesis of Tri-metallic layered double hydroxides (NiZnAl-LDHs): Adsorption of Rhodamine-B and methyl orange from water. *Inorg. Chem. Commun.* **2022**, *145*, 110008. [CrossRef]

3. Zhu, X.D.; Pei, L.X.; Zhu, R.R.; Jiao, Y.; Tang, R.Y.; Feng, W. Preparation and characterization of Sn/La co-doped TiO_2 nanomaterials and their phase transformation and photocatalytic activity. *Sci. Rep.* **2018**, *8*, 12387. [CrossRef]

4. Cadenbach, T.; Benitez, M.J.; Tirado, S.A.; Herrera, V.O.; Debut, A.; Vizuete, K. Adsorption enhanced photocatalytic degradation of Rhodamine B using $Gd_xBi_{1-x}FeO_3$@SBA-15 (x = 0, 0.05, 0.10, 0.15) nanocomposites under visible light irradiation. *Ceram. Int.* **2021**, *47*, 29139–29148. [CrossRef]

5. Zhang, J.Y.; Tong, H.J.; Pei, W.K.; Liu, W.H.; Shi, F.Y.; Li, Y.; Huo, Y.N. Integrated photocatalysis-adsorption-membrane separation in rotating reactor for synergistic removal of RhB. *Chemosphere* **2021**, *270*, 129424. [CrossRef]

6. Kundu, B.K.; Han, G.Q.; Sun, Y.J. Derivatized benzothiazoles as two-photon-absorbing organic photosensitizers active under near infrared light irradiation. *J. Am. Chem. Soc.* **2023**, *145*, 3535–3542. [CrossRef] [PubMed]

7. Nazir, M.A.; Najam, T.; Shahzad, K.; Wattoo, M.A.; Hussain, T.; Tufail, M.K.; Shah, S.S.A.; Rehman, A.U. Heterointerface engineering of water stable ZIF-8@ZIF-67: Adsorption of rhodamine B from water. *Surf. Interfaces* **2022**, *34*, 102324. [CrossRef]

8. Jamshaid, M.; Nazir, M.A.; Najam, T.; Shah, S.S.A.; Khan, H.M.; Rehman, A.U. Facile synthesis of Yb^{3+}-Zn^{2+} substituted M type hexaferrites: Structural, electric and photocatalytic properties under visible light for methylene blue removal. *Chem. Phys. Lett.* **2022**, *805*, 139939. [CrossRef]

9. Yuan, L.; Geng, Z.Y.; Zhang, S.; Xu, J.K.; Guo, F.; Kundu, B.K.; Han, C. Efficient all-in-one removal of total chromium over nonconjugated polymer-inorganic $ZnIn_2S_4$ semiconductor hybrid. *J. Colloid Interface Sci.* **2022**, *628*, 100–108. [CrossRef]

10. Alkorbi, A.S.; Javed, H.M.A.; Hussain, S.; Lati, S.; Mahr, M.S.; Mustafa, M.S.; Alsaiari, R.; Alhemiary, N.A. Solar light-driven photocatalytic degradation of methyl blue by carbon-doped TiO_2 nanoparticles. *Opt. Mater.* **2022**, *127*, 112259. [CrossRef]

11. Tashkandi, N.Y.; Albukhari, S.M.; Ismail, A.A. Mesoporous TiO_2 enhanced by anchoring Mn_3O_4 for highly efficient photocatalyst toward photo-oxidation of ciprofloxacin. *Opt. Mater.* **2022**, *127*, 112274. [CrossRef]

12. Ortelli, S.; Vespignani, M.; Zanoni, I.; Blosi, M.; Vineis, C.; Piancastelli, A.; Baldi, G.; Dami, V.; Albonetti, S.; Costa, A.L. Design of TiO_2-surfactin hybrid systems with multifunctional properties. *Molecules* **2023**, *28*, 1863. [CrossRef]

13. Lu, N.; Cai, J.Z.; Niu, B.L.; Zhou, Y.; Zhao, G.H. Preferential removal of phthalic esters by photocatalysis on selective TiO_2. *Chem. Eng. J.* **2023**, *460*, 141735.

14. Feng, X.T.; Gu, L.F.; Wang, N.Y.; Pu, Q.S.; Liu, G.L. Fe/N co-doped nano-TiO_2 wrapped mesoporous carbon spheres for synergetically enhanced adsorption and photocatalysis. *J. Mater. Sci. Technol.* **2023**, *135*, 54–64. [CrossRef]

15. Hu, X.L.; Li, C.Q.; Song, J.Y.; Zheng, S.L.; Sun, Z.M. Hierarchical assembly of visible-light-driven Bi_2MoO_6/TiO_2/sepiolite composite for effective formaldehyde removal. *Appl. Clay Sci.* **2022**, *227*, 106590. [CrossRef]

16. Zhang, J.J.; Tan, H.B.; Deng, X.F.; Li, M.G.; Jian, S.W.; Li, G.Y. Preparation of organic montmorillonite supported TiO_2 and its application in methylene blue removal. *Constr. Build. Mater.* **2022**, *341*, 127762. [CrossRef]

17. Li, Z.Y.; He, J.L.; Ma, H.F.; Zang, L.H.; Li, D.; Guo, S.Z.; Ci, Y.H. Preparation of heterogeneous TiO_2/g-C_3N_4 with a layered mosaic stack structure by use of montmorillonite as a hard template approach: TC degradation, kinetic, mechanism, pathway and DFT investigation. *Appl. Clay Sci.* **2021**, *207*, 106107. [CrossRef]

18. Chkirida, S.; Zari, N.; Achour, R.; Hassoune, H.; Lachehab, A.; Qaiss, A.E.K.; Bouhfid, R. Highly synergic adsorption/photocatalytic efficiency of Alginate/Bentonite impregnated TiO_2 beads for wastewater treatment. *J. Photochem. Photobiol. A* **2021**, *412*, 113215. [CrossRef]

19. Pan, X.F.; Gao, H.L.; Lu, Y.; Wu, C.Y.; Wu, Y.D.; Wang, X.Y.; Pan, Z.Q.; Dong, L.; Song, Y.H.; Cong, H.P.; et al. Transforming ground mica into high-performance biomimetic polymeric mica film. *Nat. Commun.* **2018**, *9*, 2974. [CrossRef] [PubMed]

20. Li, Y.; Sun, H.J.; Peng, T.J.; You, H.; Qin, Y.T.; Zeng, L. Effects of muscovite matrix on photocatalytic degradation in TiO_2/muscovite nanocomposites. *Appl. Clay Sci.* **2019**, *179*, 105155. [CrossRef]

21. Wang, N.; Zhao, Z.T.; Liu, L.; Xing, J.J. Preparation of muscovite/tungsten-doped TiO_2 composites for the efficient photocatalytic degradation of methyl orange under simulated solar light irradiation. *Inorg. Chem. Commun.* **2022**, *138*, 109285. [CrossRef]

22. Chen, X.Y.; Liu, E.D.; Zhang, D.F.; Zhang, Z.D.; Dong, Q.; Zhang, X.Y.; Ding, X.Y.; Chen, S.H.; Zhu, X.D. Synthesis of novel muscovite loaded nano Ag/Cu_{2-x}-Fe_xO composites with excellent visible-light responsive photocatalysis. *Opt. Mater.* **2022**, *124*, 112002. [CrossRef]

23. Zhang, Y.; Wang, T.; Zhou, M.; Wang, Y.; Zhang, Z.M. Hydrothermal preparation of Ag-TiO_2 nanostructures with exposed {001}/{101} facets for enhancing visible light photocatalytic activity. *Ceram. Int.* **2017**, *43*, 3118–3126. [CrossRef]

24. Mishra, S.; Chakinala, N.; Chakinala, A.G.; Surolia, P.K. Photocatalytic degradation of methylene blue using monometallic and bimetallic Bi-Fe doped TiO_2. *Catal. Commun.* **2022**, *171*, 106518. [CrossRef]

25. Akhter, P.; Nawaz, S.; Shafiq, I.; Nazir, A.; Shafique, S.; Jamil, F.; Park, Y.K.; Hussain, M. Efficient visible light assisted photocatalysis using ZnO/ TiO_2 nanocomposites. *Mol. Catal.* **2023**, *535*, 112896. [CrossRef]

26. Bamola, P.; Sharma, M.; Dwivedi, C.; Singh, B.; Ramakrishna, S.; Dalapati, G.K.; Sharma, H. Interfacial interaction of plasmonic nanoparticles (Ag, Au) decorated floweret TiO_2 nanorod hybrids for enhanced visible light driven photocatalytic activity. *Mater. Sci. Eng. B* **2021**, *273*, 115403. [CrossRef]

27. Zhang, Z.; Yates, J.T. Band bending in semiconductors: Chemical and physical consequences at surfaces and interfaces. *Chem. Rev.* **2012**, *112*, 5520–5551. [CrossRef] [PubMed]

28. Wang, H.L.; Zhang, L.S.; Chen, Z.G.; Hu, J.Q.; Li, S.J.; Wang, Z.H.; Liu, J.S.; Wang, X.C. Semiconductor heterojunction photocatalysts: Design, construction, and photocatalytic performances. *Chem. Soc. Rev.* **2014**, *43*, 5234–5244. [CrossRef]

29. Chen, Q.F.; Wang, K.Y.; Gao, G.M.; Ren, J.Z.; Duan, R.; Fang, Y.F.; Hu, X. Singlet oxygen generation boosted by Ag-Pt nanoalloy combined with disordered surface layer over TiO$_2$ nanosheet for improving the photocatalytic activity. *Appl. Surf. Sci.* **2021**, *538*, 147944. [CrossRef]

30. Bai, S.; Jiang, J.; Zhang, Q.; Xiong, Y.J. Steering charge kinetics in photocatalysis: Intersection of materials syntheses, characterization techniques and theoretical simulations. *Chem. Soc. Rev.* **2015**, *44*, 2893. [CrossRef]

31. Sun, Z.G.; Liu, C.Y.; Li, X.S.; Fang, Y.R.; Zhu, X.B.; Zhu, A.M. Semi-transparent nanofilms of plasmonic Au/TiO$_2$ for visible-light photocatalysis. *Mater. Chem. Phys.* **2022**, *280*, 125773. [CrossRef]

32. Zhu, X.D.; Qin, F.Q.; Xia, Y.W.; Yang, D.X.; Feng, W.; Jiao, Y. Three-phase mixed titania powder modified by silver and silver chloride with enhanced photocatalytic activity under UV–visible light. *Nanomaterials* **2022**, *12*, 1599. [CrossRef] [PubMed]

33. Michalska, M.; Pavlovský, J.; Lemański, K.; Małecka, M.; Ptak, M.; Novák, V.; Kormunda, M.; Matějka, V. The effect of surface modification with Ag nanoparticles on 21 nm TiO$_2$: Anatase/rutile material for application in photocatalysis. *Mater. Today Chem.* **2022**, *26*, 101123. [CrossRef]

34. Yaacob, N.; Ismail, A.F.; Sean, G.P.; Nazri, N.A.M. Structural and photocatalytic properties of co-doped hybrid ZrO$_2$-TiO$_2$ photocatalysts. *SN Appl. Sci.* **2019**, *1*, 252. [CrossRef]

35. Zhu, X.D.; Qin, F.Q.; Xia, Y.W.; Zhong, Y.Y.; Zhang, X.P.; Feng, W.; Jiao, Y. Synthesis of Ag@AgCl modified anatase/rutile/brookite mixed phase TiO$_2$ and their photocatalytic property. *Nanotechnol. Rev.* **2022**, *11*, 2916–2927. [CrossRef]

36. Ma, H.C.; Zheng, W.B.; Yan, X.; Li, S.Z.; Zhang, K.; Liu, G.J.; Jiang, L. Polydopamine-induced fabrication of Ag-TiO$_2$ hollow nanospheres and their application in visible-light photocatalysis. *Colloids Surf. A* **2020**, *586*, 124283. [CrossRef]

37. Tian, M.Q.; Wang, J.J.; Sun, R.J.; Lu, D.Z.; Li, N.; Liu, T.J.; Yao, M.; Zhang, G.Q.; Li, L.B. Facile synthesis of rod-like TiO$_2$-based composite loaded with g-C$_3$N$_4$ for efficient removal of high-chroma organic pollutants based on adsorption-photocatalysis mechanism. *Inorg. Chem. Commun.* **2022**, *141*, 109517. [CrossRef]

38. Ren, Y.W.; Xing, S.; Wang, J.; Liang, Y.; Zhao, D.Y.; Wang, H.L.; Wang, N.; Jiang, W.W.; Wu, S.M.; Liu, S.M.; et al. Weak-light-driven Ag-TiO$_2$ photocatalyst and bactericide prepared by coprecipitation with effective Ag doping and deposition. *Opt. Mater.* **2022**, *124*, 111993. [CrossRef]

39. Zhu, X.D.; Liu, H.; Wang, J.; Dai, H.L.; Bai, Y.; Feng, W.; Han, S.H. Investigation of photocatalytic activity of Ag-rutile heterojunctions. *Micro Nano Lett.* **2020**, *15*, 1130–1133. [CrossRef]

40. Zhu, X.D.; Qin, F.Q.; He, L.L.; Jiao, Y.; Feng, W. Enhanced photocatalytic activity of anatase/rutile heterojunctions by lanthanum and tin co-doping. *Int. J. Mol. Sci.* **2022**, *23*, 11339. [CrossRef]

41. Sun, Y.; Gao, Y.; Zeng, J.Y.; Guo, J.; Wang, H. Enhancing visible-light photocatalytic activity of Ag-TiO$_2$ nanowire composites by one-step hydrothermal process. *Mater. Lett.* **2020**, *279*, 128506. [CrossRef]

42. Liang, C.X.; Li, C.T.; Zhu, Y.C.; Du, X.Y.; Zeng, Y.F.; Zhou, Y.H.; Zhao, J.G.; Li, S.H.; Liu, X.; Yu, Q.; et al. Light-driven photothermal catalysis for degradation of toluene on CuO/TiO$_2$ Composite: Dominating photocatalysis and auxiliary thermalcatalysis. *Appl. Surf. Sci.* **2022**, *601*, 154144. [CrossRef]

43. Zhu, X.D.; Zhu, R.R.; Pei, L.X.; Liu, H.; Xu, L.; Wang, J.; Feng, W.; Jiao, Y.; Zhang, W.M. Fabrication, characterization, and photocatalytic activity of anatase/rutile/SnO$_2$ nanocomposites. *J. Mater. Sci. Mater. Electron.* **2019**, *30*, 21210–21218. [CrossRef]

44. Zhou, Z.Y.; Zhu, Y.M.; Jin, J.P.; Han, Y.X.; Bai, Z.; Tang, Z.D. Enhanced vanadium extraction from Muscovite-type Vanadium-bearing shale by suspension oxidation roasting pretreatment-acid leaching. *Sep. Purif. Technol.* **2023**, *309*, 123066. [CrossRef]

45. Bao, N.; Wei, Z.T.; Ma, Z.H.; Liu, F.; Yin, G.B. Si-doped mesoporous TiO$_2$ continuous fibers: Preparation by centrifugal spinning and photocatalytic properties. *J. Hazard. Mater.* **2010**, *174*, 129–136. [CrossRef]

46. Peng, F.P.; Ni, Y.R.; Zhou, Q.; Kou, J.H.; Lu, C.H.; Xu, Z.Z. New g-C$_3$N$_4$ based photocatalytic cement with enhanced visible-light photocatalytic activity by constructing muscovite sheet/SnO$_2$ structures. *Constr. Build. Mater.* **2018**, *179*, 315–325. [CrossRef]

47. Jia, T.K.; Fu, F.; Yu, D.S.; Cao, J.L.; Sun, G. Facile synthesis and characterization of N-doped TiO$_2$/C nanocomposites with enhanced visible-light photocatalytic performance. *Appl. Surf. Sci.* **2018**, *430*, 438–447. [CrossRef]

48. Deng, J.L.; Gao, J.; Liu, M.; Zheng, L.C.; Wang, Y.F.; Wang, Y.Q.; Chen, C.Z.; Li, Y.; He, G.; Liu, Y. Construction of Z-scheme TiO$_2$/Ag/ZIF-8 nanorod array film with boosting photocatalytic and photoelectrochemical properties. *J. Alloys Compd.* **2023**, *932*, 167680. [CrossRef]

49. Lam, S.M.; Sin, J.C.; Abdullah, A.Z.; Mohamed, A.R. Investigation on visible-light photocatalytic degradation of 2,4-dichlorophenoxyacetic acid in the presence of MoO$_3$/ZnO nanorod composites. *J. Mol. Catal. A Chem.* **2013**, *370*, 123–131. [CrossRef]

50. Li, J.L.; Zhang, M.; Guan, Z.J.; Li, Q.Y.; He, C.Q.; Yang, J.J. Synergistic effect of surface and bulk single-electron-trapped oxygen vacancy of TiO$_2$ in the photocatalytic reduction of CO$_2$. *Appl. Catal. B-Environ.* **2017**, *206*, 300–307. [CrossRef]

51. Yang, Q.L.; Hu, M.Y.; Guo, J.; Ge, Z.H.; Feng, J. Synthesis and enhanced photocatalytic performance of Ag/AgCl/TiO$_2$ nanocomposites prepared by ion exchange method. *J. Mater.* **2018**, *4*, 402–411. [CrossRef]

52. Li, J.R.; Jin, Z.Z.; Zhang, Y.M.; Liu, D.; Ma, A.J.; Sun, Y.M.; Li, X.Y.; Cai, Q.; Gui, J.Z. Ag-induced anatase-rutile TiO$_{2-x}$ heterojunction facilitating the photogenerated carrier separation in visible-light irradiation. *J. Alloys Compd.* **2022**, *909*, 164815. [CrossRef]

53. Wei, Z.D.; Xu, M.Q.; Liu, J.Y.; Guo, W.Q.; Jiang, Z.; Shangguan, W.F. Simultaneous visible-light-induced hydrogen production enhancement and antibiotic wastewater degradation using MoS$_2$@Zn$_x$Cd$_{1-x}$S: Solid-solution-assisted photocatalysis. *Chin. J. Catal.* **2020**, *41*, 103–113. [CrossRef]

54. Reddy, N.K.; Reddy, K.T.R. Optical behaviour of sprayed tin sulphide thin films. *Mater. Res. Bull.* **2006**, *41*, 414–422. [CrossRef]

55. Zhu, X.D.; Xu, H.Y.; Yao, Y.; Liu, H.; Wang, J.; Pu, Y.; Feng, W.; Chen, S.H. Effects of Ag^0-modification and Fe^{3+}-doping on the structural, optical and photocatalytic properties of TiO_2. *RSC Adv.* **2019**, *9*, 40003–40012. [CrossRef] [PubMed]

56. Yang, Z.L.; Lu, J.; Ye, W.C.; Yu, C.S.; Chang, Y.L. Preparation of Pt/TiO_2 hollow nanofibers with highly visible light photocatalytic activity. *Appl. Surf. Sci.* **2017**, *392*, 472–480. [CrossRef]

57. Gao, X.T.; Zhang, S.; Liu, J.C.; Xu, S.Q.; Li, Z.H. Enhanced active oxidative species generation over Fe-doped defective TiO_2 nanosheets for boosted photodegradationt. *Rsc Adv.* **2020**, *10*, 40619–40624. [CrossRef]

58. Zhu, X.D.; Wang, J.; Yang, D.X.; Liu, J.W.; He, L.L.; Tang, M.; Feng, W.; Wu, X.Q. Fabrication, characterization and high photocatalytic activity of Ag-ZnO heterojunctions under UV-visible light. *Rsc Adv.* **2021**, *11*, 27257–27266. [CrossRef]

59. Celebi, N.; Aydin, M.Y.; Soysal, F.; Ciftci, Y.O.; Salimi, K. Ligand-free fabrication of Au/TiO_2 nanostructures for plasmonic hot-electron-driven photocatalysis: Photoelectrochemical water splitting and organic-dye degredation. *J. Alloys Compd.* **2021**, *860*, 157908. [CrossRef]